

# 3D Printing of Viscoelastic Suspensions via Digital Light Synthesis for Tough Nanoparticle–Elastomer Composites

Kaiyang Wang, Wenyang Pan, Zheng Liu, Thomas J. Wallin, Geoffrey van Dover, Shuo Li, Emmanuel P. Giannelis, Yigit Menguc,\* and Robert F. Shepherd\*

The rheological parameters required to print viscoelastic nanoparticle suspensions toward tough elastomers via Digital Light Synthesis (DLS) (an inverted projection stereolithography system) are reported. With a model material of functionalized silica nanoparticles suspended in a poly(dimethylsiloxane) matrix, the rheological-parameters-guided DLS can print structures seven times tougher than those formed from the neat polymers. The large yield stress and high viscosity associated with these high concentration nanoparticle suspensions, however, may prevent pressure-driven flow, a mechanism essential to stereolithography-based printing. Thus, to better predict and evaluate the printability of high concentration nanoparticle suspensions, the boundary of rheological properties compatible with DLS is defined using a non-dimensional Peclet number ( $Pe$ ). Based on the proposed analysis of rheological parameters, the border of printability at standard temperature and pressure (STP) is established by resin with a silica nanoparticle mass fraction ( $\phi_{\text{silica}}$ ) of 0.15. Above this concentration, nanoparticle suspensions have  $Pe > 1$  and are not printable. Beyond STP, the printability can be further extended to  $\phi_{\text{silica}} = 0.20$  via a heating module with lower shear rate to reduce the  $Pe < 1$ . The printed rubber possesses even higher toughness ( $\Gamma \approx 155 \text{ kJ m}^{-3}$ ), which is 40% higher over that of  $\phi_{\text{silica}} = 0.15$ .

Silicone elastomers such as poly(dimethylsiloxane) (PDMS) are an important class of soft materials. They are relatively inert, non-toxic, thermally stable, with very low glass transition temperatures ( $T_g \approx -120 \text{ }^\circ\text{C}$ ). Their material properties can also be

easily tuned by copolymerization with other polymers such as polyurethane, polyester, and polyamide,<sup>[1–3]</sup> or via surface modification and forming composite materials for myriad applications.<sup>[4–11]</sup>

Due to these advantages, synthetic silicone not only finds broad implementations in construction and automotive industry, but also has been adopted by many emergent research fields such as microfluidics, soft robotics, wearable electronics, and biomedical applications.<sup>[12–15]</sup> As these application spaces grow in importance, they also require more sophisticated, high precision 3D architectures.<sup>[16]</sup> Reliable and rapid 3D printing of tough and resilient silicone elastomers, therefore, needs to be developed to replace traditional, low efficiency replica molding of such materials. Toward this goal, recent works have shown high quality 3D printing via stereolithography (SLA) of silicone formulations based on thiol–ene, thiol–acrylate, or acrylate-functionalized polysiloxanes.<sup>[17–19]</sup> Although

they can be printed, these PDMS networks possess mechanical properties (tensile strength,  $\sigma < 0.8 \text{ MPa}$ ; ultimate elongation,  $\gamma_{\text{ult}} < 4.5$ ; and toughness,  $\Gamma < 40 \text{ kJ m}^{-3}$ ) well below those of commercial liquid silicone rubber (LSR) counterparts, such as Ecoflex 00–30 (Smooth-On, Inc.;  $\sigma > 1.3 \text{ MPa}$ ,  $\gamma_{\text{ult}} \approx 9$ ).<sup>[20]</sup> As a potential solution, incorporating nanofillers to the silicone matrix can enhance tangent modulus ( $E$ ) and ultimate elongation ( $\gamma_{\text{ult}}$ ) of these materials.<sup>[21]</sup> This reinforcement relies on the interactions between the siloxane backbone and the filler nanoparticles (typically silica, or  $\text{SiO}_2$ ). The local stress induced by nanoparticles, even at low concentrations, can effectively inhibit crack propagation, allowing for larger  $\gamma_{\text{ult}}$ .<sup>[22–25]</sup> Many commercial silicones based on LSR and RTV (Room Temperature Vulcanization), such as Silopren\* LSR (Momentive Performance Materials, Inc.) and SilGel (Wacker Chemie AG), derive their superior properties from these nanoparticle–elastomer interactions, in some cases with high mass fractions  $\phi_{\text{silica}} > 0.30$ .<sup>[26–28]</sup>


Numerous variations of SLA exist with the main distinctions arising from the chosen method of illumination (e.g., laser raster scanning, two-photon polymerization, image projection) and build direction (e.g., top-down, bottom-up). The use of high loadings (i.e.,  $\phi_{\text{silica}} > 0.10$ ) of nanoparticles for toughening involves a broader problem for SLA. The apparent viscosity,  $\mu_{\text{app}}$ , of colloidal suspensions rises rapidly with increasing

K. Wang, Dr. W. Pan, S. Li, Prof. E. P. Giannelis, Prof. R. F. Shepherd  
Department of Materials Science and Engineering  
Cornell University  
Ithaca, NY 14853, USA  
E-mail: rfs247@cornell.edu

Z. Liu, Prof. R. F. Shepherd  
Sibley School of Mechanical and Aerospace Engineering  
Cornell University  
Ithaca, NY 14853, USA

Dr. T. J. Wallin, Dr. Y. Menguc  
Facebook Reality Labs  
Redmond, WA 98052, USA  
E-mail: softrobot@fb.com

G. van Dover  
Department of Chemistry  
St. Olaf College  
Northfield, MN 55057, USA

 The ORCID identification number(s) for the author(s) of this article can be found under <https://doi.org/10.1002/adma.202001646>.

DOI: 10.1002/adma.202001646

loading of nanoparticles,<sup>[29]</sup> and can easily be in excess of  $\mu_{app} \approx 200$  Pa s. In contrast, top-down SLA, where the part is photoirradiated from above and pulled down into the vat of liquid resin, has been reported to require low apparent viscosities,  $\mu_{app} < 5$  Pa s experimentally,<sup>[30–32]</sup> and a complex viscosity of  $\mu^* < 42$  Pa s via simulation for specific conditions. Further, these conditions are for Newtonian fluids and do not consider the additional complication of yield stress.<sup>[33]</sup> Although viscosity could be lowered by adding diluent, the resulting product will have lower gel fraction or require much longer time to polymerize.<sup>[34,35]</sup> Another challenge of printing high concentration of nanoparticles is the onset of a yield stress ( $\tau_y$ ) required to cause the liquid resin to flow. For top-down SLA, the hydrostatic pressure in the recoating process is only about 1 Pa assuming layer thickness of roughly 100  $\mu\text{m}$  (see Supporting Information for calculation).

In bottom-up SLA, light passes through a transparent window at the base of a vat of resin to photopolymerize or photocrosslink an object. Often, the printed part adheres to the build window and must be sheared off by a horizontal translation prior to raising the build-head to the next layer. In either method, sweeping a wiper blade across the liquid resin can provide a uniform coating of viscous resin when the hydrostatic pressure is insufficient. Even so, printing composite resins with  $\mu_{app}$  above 5 Pa s remains a major challenge.<sup>[36]</sup>

Recent hardware advances in bottom-up printers can prevent adhesion between the build window and the printed object, enabling continuous movement of the build-head without the need for shear detachment of each layer (often referred to as

Continuous Liquid Interface Production, CLIP, or High Area Rapid Printing, HARP; **Figure 1a**).<sup>[37,38]</sup> As most early works emphasized on increasing build speeds, we now demonstrate that continuous bottom-up SLA (referred to as Digital Light Synthesis, i.e., DLS, from here on) can also use pressure-driven flow for resin replenishment. During DLS, the printed part remains immersed inside uncured resin, creating a low-pressure zone under the previously printed layers when the build-head is moved up (**Figure 1a, inset**). Using this pressure difference to induce flow, we can print high concentrations of silica nanoparticle,  $\phi_{silica} > 0.15$ , suspended in PDMS prepolymers. At  $\phi_{silica} > 0.15$ , these suspensions behave like pastes, with three orders of magnitudes higher viscosity ( $\mu_{app} \approx 60$  Pa s) than that of the neat resin. The advantages of printing these highly viscoelastic suspensions, however, are obvious;  $\phi_{silica} = 0.15$  has an increased  $\gamma_{ult}$  of  $\approx 50\%$  and an increased  $\Gamma$  of  $\approx 600\%$  over neat silicone (**Figure 1b**). There is, however, a rheological limit to the  $\phi_{silica}$  we can incorporate for our particular material choice at standard temperature and pressure (STP).

Because any polymer matrix presently printed via DLS can benefit from the addition of high concentrations of nanoparticles,<sup>[39,40]</sup> and the resulting increase in viscosity and yield stress will present a limit to DLS, we applied non-dimensional analysis of the rheological parameters to predict the printability of these classes of resins. Furthermore, we modified a commercial SLA printer equipped with heating modules that allows us to adjust these parameters beyond the boundaries set by printing at STP. With such improvement, we can now print photopolymer resin with even higher  $\phi_{silica} = 0.20$  ( $\mu_{app} \approx 200$  Pa s,  $\tau_y \approx 10$  Pa) for

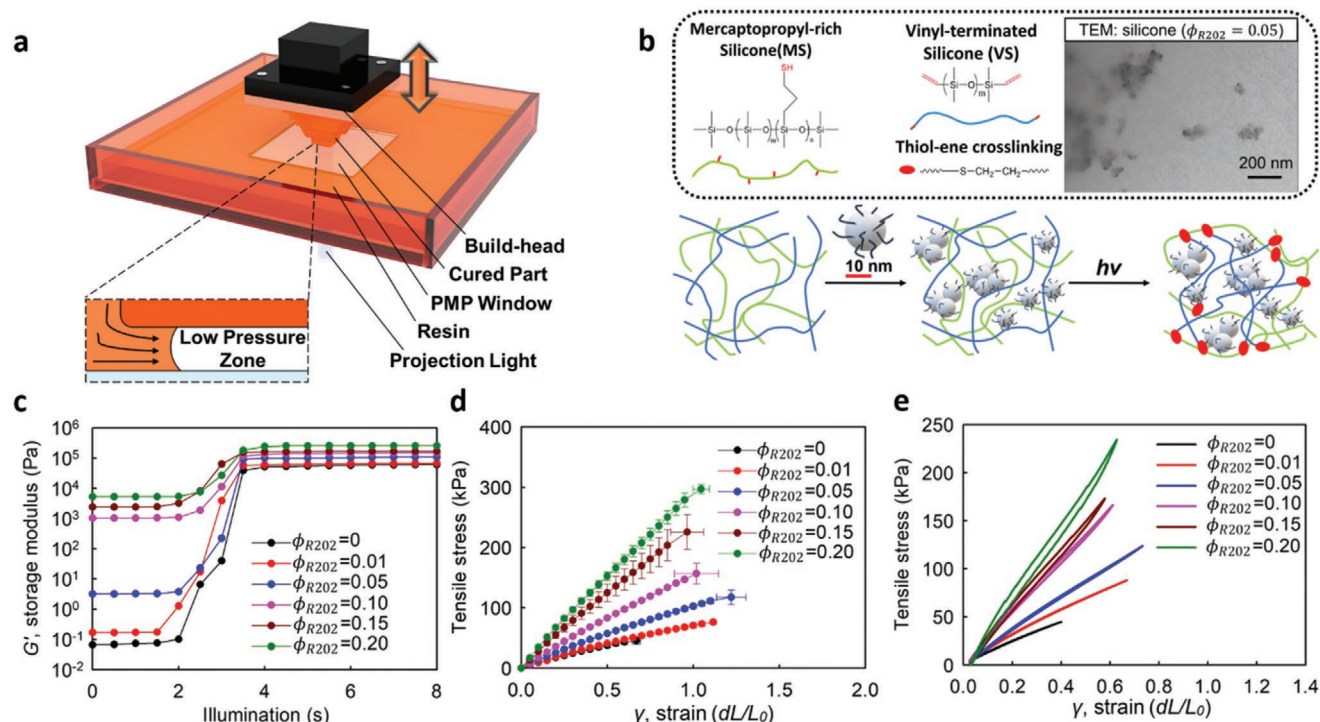


**Figure 1.** Printer setup and resin design. a) Schematic illustration of the continuous bottom-up stereolithography (DLS), with the arrow indicating motion directions of the build-head. b) Photochemistry of the 3D printable silicone nanocomposite, with TEM images of  $\phi_{R202} = 0.05$  silicone. c) Photorheological comparison of the neat 5% VS6000 resin and different suspensions. d) Uniaxial tensile tests of the cured silicone nanocomposites. e) First cycle of silicone nanocomposites from cyclic tensile tests, where the strain range is 0 to 0.6  $\gamma_{ult}$ .

structures with even higher toughness ( $\Gamma \approx 155 \text{ kJ m}^{-3}$ ; 40% higher compared to  $\phi_{\text{silica}} = 0.15$ ).

In the preliminary experiments, we compared nontreated fumed silica species with a few hydrophobic Evonik Aerosil fumed silica (R202, R812, and R972) to select the most stable nanofiller for the photocurable siloxanes. Initially, we mixed  $\phi_{\text{silica}} = 0.01$  of each silica species in the silicone matrix (5% VS6000). Only the R202 (PDMS coated silica) filled silicone showed a significantly improved storage modulus ( $G'$ ) in a strain amplitude rheological measurement (Figure S1a,b, Supporting Information). The transmission electron microscopy (TEM) image also confirmed good dispersion of R202 with aggregates ranging from 50 nm to 500 nm (Figure 1b). This observed filler size is also consistent with the TEM images and the observed size of original silica aggregates formed in the flame, as reported by Aerosil.<sup>[44]</sup> The direct blending is relatively easy and cost efficient compared with in situ synthesis of fillers through sol-gel process from precursors absorbed in the polymer melt.<sup>[25,42]</sup>

To investigate the effects of nanofillers on photochemistry, we performed photorheology and photo-differential scanning calorimetry (photo-DSC). From the photorheology measurements, we did not observe a significant difference in the gelation speed of the suspensions, given their different initial apparent viscosity (measuring frequency,  $f = 1 \text{ s}^{-1}$  and strain,  $\gamma = 0.01$ ). All specimens have  $G'$  quickly reaching a plateau after 3.5 s illumination from a light source with intensity of  $10 \text{ mW cm}^{-2}$  (with photoirradiation dosage,  $\Omega \approx 35 \text{ mJ cm}^{-2}$ ; Figure 1c). In addition, the photo-DSC experiments recorded near identical exothermal peaks from the neat 5% VS6000, and nanoparticle suspensions, indicating that R202 silica does not affect the photochemistry (Figure S2, Supporting Information).

We further evaluated the resulting mechanical properties by varying the R202 loading, up to  $\phi_{\text{R202}} = 0.20$ . Results from uniaxial tensile tests suggest a significantly improved toughness with increasing  $\phi_{\text{R202}}$  when compared to the neat 5% VS6000 silicone (Figure 1d). We found the tangent modulus ( $E$ , measured at  $\gamma = 0.10$ ) had a linear correlation with  $\phi_{\text{R202}}$  (Figure S3, Supporting Information), which is consistent with previously reported results.<sup>[43]</sup> This significantly increased  $E$  reveals good dispersion and interfacial interactions between the nanoparticles and the elastomer matrix.<sup>[44]</sup> Though it is clear from the vast amount of literature on 3D printing that printed parts typically have different mechanical properties than molded ones, we chose to perform the majority of mechanical testing on molded tensile coupons. The reduced time to fabricate and test, as well as improved uniformity of parts allow us to get better statistical information for comparing the effect of silica loading. For comparison between printed and molded mechanical properties, we print several tensile coupons of our highest  $\phi_{\text{R202}}$ .

In cyclic tensile tests, we observed nearly identical loading and unloading curves (cycles 1–9; Figure 1e) after the initial training cycle (cycle 0, Figure S4, Supporting Information, to erase the Mullins effect).<sup>[22,45]</sup> The work of extension increases with  $\phi_{\text{R202}}$ , along with a slight decrease in resilience, as noted by the formation of a slightly larger hysteretic loop.

The pressure-driven flow, however, only works under the condition of continuous resin flow. This condition requires

the fluid flows at the appropriate timescales (set by  $\mu_{\text{app}}$ ) and is sheared in excess of  $\tau_y$ . As shown in Figure 2a,  $\mu_{\text{app}}$  of the resin shows typical behavior of shear thinning colloidal gels, with the dashed lines indicating fitting results of Herschel–Bulkley model.<sup>[46,47]</sup> As  $\phi_{\text{R202}}$  gets higher, the viscosity of the resin increases drastically. For example, at shear rate  $\dot{\gamma} = 1 \text{ s}^{-1}$ , a  $\phi_{\text{R202}} = 0.20$  suspension has  $\mu_{\text{app}} \approx 200 \text{ Pa s}$ , whereas the  $\mu_{\text{app}}$  of the neat 5% VS6000 resin is about  $0.1 \text{ Pa s}$ . Figure 2a, inset shows  $\phi_{\text{R202}} = 0.15$  suspension in a 20 mL glass vial, indicating little evidence of flowing after being held upside down for more than 30 s. For resins with high  $\phi_{\text{R202}}$ , the data under high shear rate is hard to obtain due to flow instability and fluid fracture; therefore, we were unable to directly obtain viscometry data of  $\phi_{\text{R202}} = 0.15$  for  $\dot{\gamma} \gtrsim 10^2 \text{ s}^{-1}$  and  $0.20$  for  $\dot{\gamma} \gtrsim 10^1 \text{ s}^{-1}$ .

To assess the boundaries of viscoelastic printing, we estimated the yield stress of increasing  $\phi_{\text{R202}}$  suspensions at the  $G'$  and  $G''$  crossover (Figure 2b). As  $\phi_{\text{R202}}$  monotonically increases, larger stress is required to yield the fluid (e.g., when  $\phi_{\text{R202}} = 0.15$ ,  $\tau_y$  is  $\approx 6 \text{ Pa}$ ; Figure 2c), resulting in a dependence of  $\tau_y \propto \phi_{\text{R202}}^{2.34}$ . This dependence is consistent with the fractal geometry of particulate aggregates and their influence on yield stress.<sup>[48,49]</sup> Using DLS, however,  $\phi_{\text{R202}} = 0.15$  can be successfully printed.

At  $\phi_{\text{R202}} = 0.20$ , the native DLS pressure-driven flow is insufficient to recoat the resin vat for printing (Figure S5, Supporting Information). In this case, we hypothesize that fluid fracture occurs due to the viscoelasticity of the suspensions and practical choice of build-head rate. When the flow stress is applied faster than it can be dissipated, fluid fracture occurs that breaks the seal between resin and build-head, which severs the pressure-driven flow. To determine the timescales associated with this flow instability, we conducted frequency sweeps for these suspensions (Figure 2d). For neat 5% VS6000 and  $\phi_{\text{R202}} = 0.01$ , the data at high frequency fluctuate and are not valid due to this flow instability.

In particulate suspensions, the characteristic timescale for particles to relieve their accumulated stress via diffusion is called the relaxation time and can be expressed by Equation (1):

$$\tau_p = \frac{\pi \mu_{\infty}' a^3}{k_B T} \quad (1)$$

where  $\mu_{\infty}'$  is the high frequency viscosity from the frequency sweep oscillatory rheology tests (Figure 2d),  $a$  is particle's diameter,  $k_B$  is Boltzmann constant, and  $T$  is temperature.<sup>[50]</sup> At high frequencies,  $G''/\omega$  ( $\omega$ , angular frequency) approaches to a constant which can be defined as  $\mu_{\infty}'$  (Figure S5, Supporting Information). From the results, relaxation time increases from  $\tau_p \approx 2.4 \times 10^{-2} \text{ s}$  to  $\tau_p \approx 4.3 \times 10^{-2} \text{ s}$  for  $\phi_{\text{R202}} = 0.15$  and  $\phi_{\text{R202}} = 0.20$ , respectively. To assess the onset of viscoelastic instabilities and fluid fracture during resin flow, we compared these relaxation times to the applied shear rate via the Peclet number ( $Pe$ ), which is defined by Equation (2):

$$Pe = \tau_p \cdot \dot{\gamma} \quad (2)$$

For  $Pe > 1$ , the relaxation time is in excess of the shear rate experienced by the fluid, and the flow will become unstable and discontinuous.<sup>[51–53]</sup>

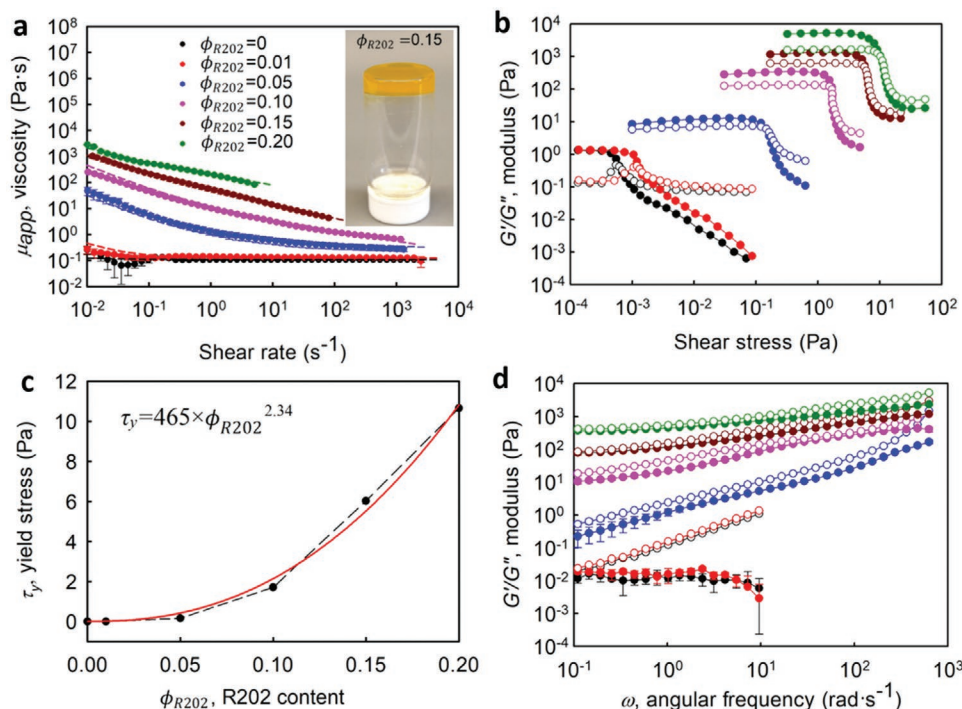


**Figure 2.** Rheological properties of silica suspensions. a) Shear viscosity of the silica-siloxane suspensions with inlet figure showing a resin demo of  $\phi_{R202} = 0.15$ . b) Oscillatory strain amplitude sweep measuring the storage modulus ( $G'$ -closed dots) and loss modulus ( $G''$ -open dots) versus shear stress of the silica suspensions. c) Yield stress ( $\tau_y$ , defined as the stress when  $G' = G''$ ) as a function of silica content ( $\phi_{R202}$ ), with the solid red line showing the exponential fitting ( $\tau_y \propto \phi_{R202}^{2.34}$ ) of yield stress with increasing  $\phi_{R202}$ . d) Frequency sweep of silica-siloxane suspensions, where closed dots represent  $G'$  and open dots represent  $G''$ .

In our experiments, the layer thickness is set as 30  $\mu\text{m}$  and the build-head moving speed is 1  $\text{mm s}^{-1}$ . Therefore, the initial shear rate resulted from the vertical motion of the build-head can be simply estimated as 33  $\text{s}^{-1}$ .<sup>[30]</sup> For printing of the resin with  $\phi_{R202} = 0.20$ , the resulting  $Pe \approx 1.4$  exceeds the criteria for flow instabilities so the pressure-driven flow is not reliable, explaining the poor print quality we observed (Figure S6, Supporting Information). This simplified model also reveals that slow build-head moving speed or thick printing layer is favorable for high viscosity resin printing. For  $\phi_{R202} = 0.20$  or higher concentrations, however, further increasing of the layer thickness will be restrained by the stronger absorption with higher silica loading (Figure S7, Supporting Information); simply reducing the build-head moving speed will increase the printing time significantly.

As shown in Figure 3, we have successfully printed silica-silicone nanocomposites up to  $\phi_{R202} = 0.15$ . We printed step pyramids for testing print resolution, with small features such as stairs on the pyramid being well preserved. We used laser confocal microscopy (LCM) to quantify surface roughness and feature resolution for different  $\phi_{R202}$ . We measured the average root mean square height,  $S_q$ , from the surface of different small stairs, as an indication for roughness. From the top view (TV), we found that the neat silicone (Figure 3a) and  $\phi_{R202} = 0.05$  (Figure 3b) possess similar roughness, while the surface of  $\phi_{R202} = 0.15$  (Figure 3c) is slightly smoother. From the front view (FV), we observed a decrease in roughness with increasing  $\phi_{R202}$ . We can, however, clearly observe the individually printed layers from the optical images for  $\phi_{R202} \leq 0.05$ , but these layers are less prominent for  $\phi_{R202} = 0.15$ . Figure 3d displays the contour of one single

stair from different demonstrations and their intended, computer-aided design (CAD) geometry. The angle between the face of the stair step in the CAD is 90°, whereas the angle becomes slightly larger with increasing  $\phi_{R202}$ . We attribute this broadening to a small amount of excess resin that is cured during printing, which may also result in overall lower  $S_q$  at increased  $\phi_{R202}$ . We further employed scanning electron microscopy (SEM) to show a magnified view for a single stair of  $\phi_{R202} = 0.15$  (Figure S8, Supporting Information) and noted that some cured material piled up at the corner. We attribute this phenomenon to the higher viscosity, as well as stronger light scattering with higher nanoparticle loading (Figure S9, Supporting Information). When we excited the suspensions at wavelength,  $\lambda \approx 410$  nm, close to the working wavelength of the Ember SLA printer ( $\lambda \approx 405$  nm), we observed obvious light scattering as a result of the suspended silica.

Based on the model we constructed (Equations (1) and (2)), we found that  $\tau_p$  or  $\dot{\gamma}$  can be effectively reduced to bring the  $Pe < 1$  for printing  $\phi_{R202} \geq 0.20$  suspensions toward even tougher silicone nanocomposites. Therefore, we developed a modified DLS system with a heating assisted module (Figure 4a) to lower  $\tau_p$  and applied slower build-head movement during DLS to reduce  $\dot{\gamma}$ . Figure 4b showed a printed pyramid of  $\phi_{R202} = 0.20$  printed at 60 °C (Figure S10, Supporting Information) and build-head speed of 0.8  $\text{mm s}^{-1}$ , with the feature of small stairs easily distinguished. To compare the mechanical properties between the printed and the molded  $\phi_{R202} = 0.20$ , we fabricated dog-bone shaped specimens and conducted tensile tests (Figure 4c). The printed samples showed smaller  $E \approx 110$  kPa but larger  $\gamma_{ult} \approx 1.5$ , which lead to an overall higher  $\Gamma \approx 220$   $\text{kJ m}^{-3}$ .

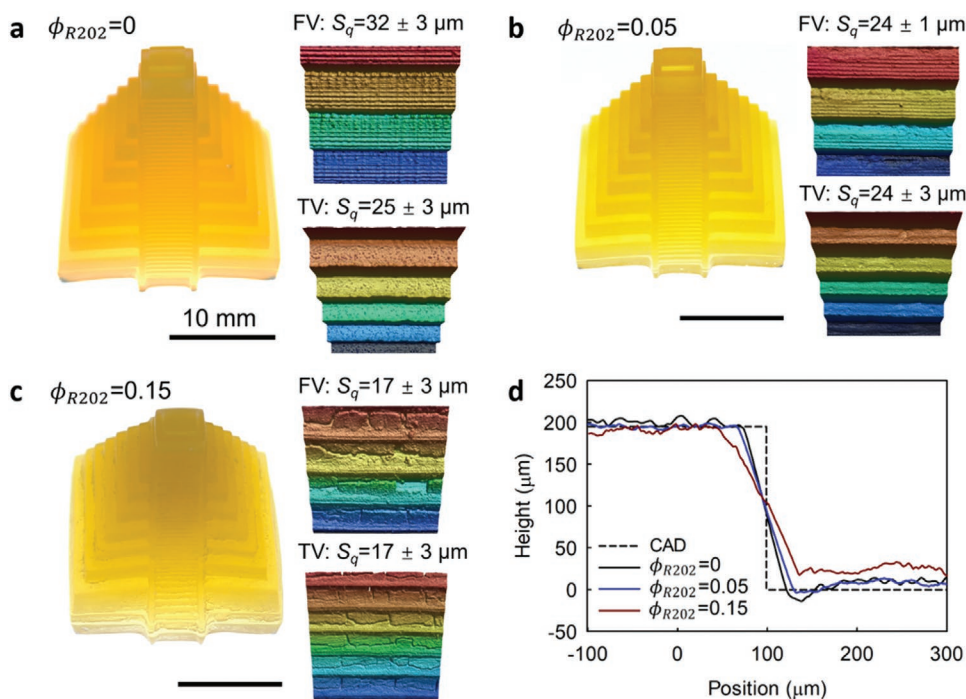


**Figure 3.** 3D printed pyramid demos via DLS. The demos are printed from neat 5% VS6000 (a),  $\phi_{R202} = 0.05$  (b) and  $\phi_{R202} = 0.15$  (c) resins. The laser confocal microscopy (LCM) images showed the front views (FV) and top views (TV) of the stairs with different surface roughness,  $S_q$ . The scale bars in the optical images represent 10 mm. d) Contour of one single stair extracted from FV images of CAD (dashed line) and different  $\phi_{R202}$ .

At an elevated temperature, we observed that  $\mu^*$  of the materials significantly decreased in the temperature sweep rheological measurements (Figure 4d), as previously reported.<sup>[54]</sup> The heat induced thinning becomes more pronounced with increasing  $\phi_{R202}$ , with a temperature thinning exponent of  $\mu^* \propto T^{-1.18}$

for  $\phi_{R202} = 0.20$  and  $\mu^* \propto T^{-0.43}$  for  $\phi_{R202} = 0$ . To calculate  $\tau_p$ , we performed frequency sweep of  $\phi_{R202} = 0.20$  from 25 to 60 °C. We found that temperature has little effect on  $\mu'_\infty$  (Figure 4e), which can be explained by time–temperature superposition.<sup>[55]</sup> Thus,  $\tau_p$  scales with  $1/kT_B$  and is reduced from  $\approx 4.3 \times 10^{-2}$  s

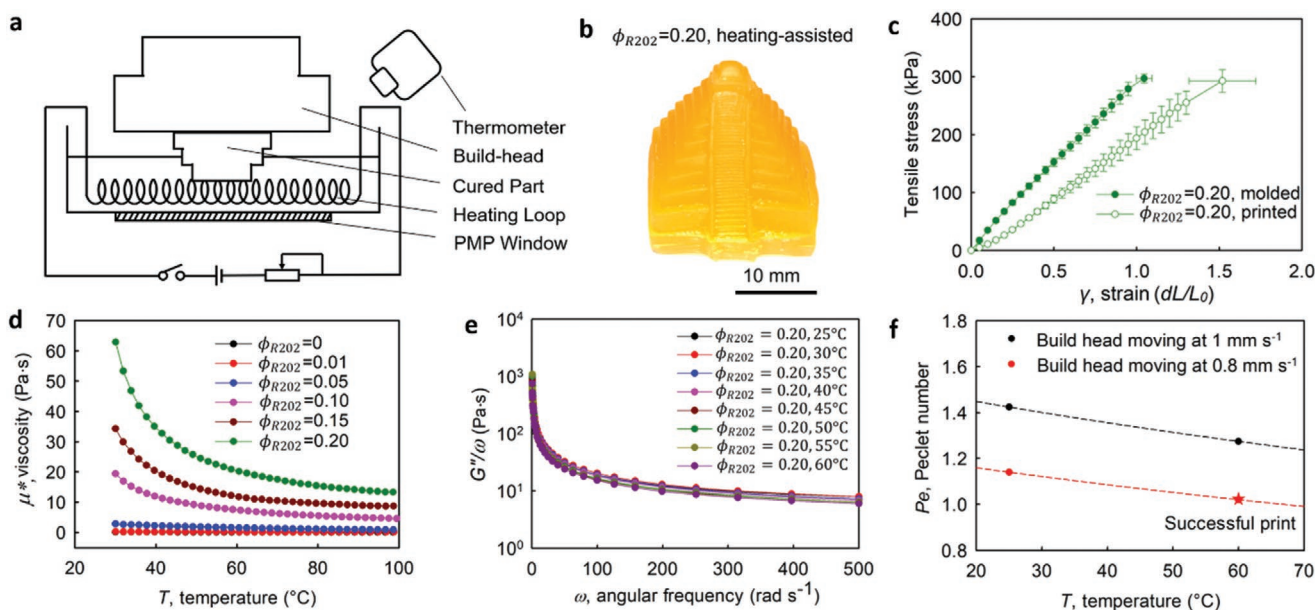


**Figure 4.** Heating assisted DLS. a) Schematic design of the heating-assisted DLS. b) A 3D printed silicone pyramid with  $\phi_{R202} = 0.20$  through heating-assisted DLS. c) Uniaxial tensile tests of molded and printed  $\phi_{R202} = 0.20$ . d) Temperature sweep of the silica–silicone suspensions with different  $\phi_{R202}$  from 30 to 100 °C. e)  $G''/\omega$  versus  $\omega$  of  $\phi_{R202} = 0.20$  under different temperatures. f) Calculated Peclet number (dashed line) with temperature for different printing speed. The parameter used for successful printing is indicated in the figure.

( $T = 25\text{ }^{\circ}\text{C}$ ) to  $\approx 3.8 \times 10^{-2}\text{ s}$  ( $T = 60\text{ }^{\circ}\text{C}$ ). We still, however, experienced issues of fluid fracture when we set build-head speed at  $1\text{ mm s}^{-1}$  at  $60\text{ }^{\circ}\text{C}$  (Figure S11, Supporting Information). To illustrate the printability of  $\phi_{R202} = 0.20$ , we calculated  $Pe$  versus  $T$  at build-head speed of  $1\text{ mm s}^{-1}$  ( $\dot{\gamma} = 33\text{ s}^{-1}$ ) and  $0.8\text{ mm s}^{-1}$  ( $\dot{\gamma} = 27\text{ s}^{-1}$ ) in Figure 4f. The parameters we used for successful print correspond to  $Pe \approx 1.0$ , which is consistent with our criteria. It should be noted that our calculation so far is based on spherical particles; in future papers, we will expand our analysis to include asymmetric and non-particulate yield stress polymeric gels.

In summary, we report the systematic investigation of printing viscoelastic suspensions with DLS. We used a model system of PDMS-functionalized silica nanoparticles suspended in a mercapto- and divinyl-siloxane prepolymer melt to show that high viscosity ( $\mu_{app} \approx 60\text{ Pa s}$ ), yield stress ( $\tau_y \approx 6\text{ Pa}$ ) fluid can be easily printed using DLS. Using pressure-driven flow, native to the DLS, we printed high concentration ( $\phi_{R202} = 0.15$ ) of silica suspension for tough silicone elastomers.

More importantly, we provide evidence toward our notion that liquid fracture in viscoelastic resins breaks the seal that is required for printing viscous materials. We lend credence to this idea by calculating the particle diffusion time,  $\tau_p$ , and using the Peclet number,  $Pe$ , to predict the onset liquid fracture. The model well illustrates the printability of our resins and sets the boundary to around  $\phi_{R202} = 0.20$  at room temperature, which agrees with our experiments. Using the principles above, we further devised a heating module to reduce  $\tau_p$ , and applied a lower build-head moving speed to lessen  $\dot{\gamma}$ , allowing us to print to at least  $\phi_{R202} = 0.20$ .

## Experimental Section

**Materials System:** Divinyl terminated polydimethylsiloxane (VS-PDMS;  $M_w \approx 6000\text{ Da}$ ) and [4–6% (mercaptopropyl)methylsiloxane]-dimethylsiloxane (MS;  $M_w \approx 7000\text{ Da}$ ) were purchased from Gelest, Inc. (Morrisville, PA, USA) and used without further treatment. They were mixed to obtain the neat resin (5% VS6000) with a stoichiometric ratio of 1 mercapto (thiol) group per 1 vinyl (-ene) group. A liquid photoinitiator blend of 20 wt% diphenyl(2,4,6-trimethylbenzoyl) phosphine oxide in 80 wt% 2-hydroxy-2-methylpropiophenone (Sigma-Aldrich Co., St. Louis, MO, USA) was added to the resins at 1 wt% concentration. Sudan I (Sigma-Aldrich, St. Louis, MO, USA) was dissolved in toluene at the concentration of  $2\text{ mg mL}^{-1}$  as a stock solution.

Fumed silica was used as the nanoparticle toughening agent, as it is composed of small aggregates that flow easily as dry powders, yet have high surface areas for toughening the polymer network.<sup>[56]</sup> Due to the historical use of fumed silica as additives in commercial silicones, there exist numerous choices for surface treatments that facilitate dispersion. To evaluate suspension stability,  $\phi_{silica} = 0.01$  dispersions of Aerosil fumed silicas (R202, R812, R7200, and R972, respectively) were created from Evonik Industries (Allentown, PA, USA) in 5% VS6000 siloxane. As expected, R202, which has a PDMS surface coating, resulted in more uniform dispersions and smaller aggregate size (50–500 nm) in the composite. Therefore, R202 was used as the nanoparticle additives throughout our 3D printing experiments.

**Resin Synthesis:** The silica nanoparticle suspensions,  $0 < \phi_{R202} \leq 0.20$ , were mixed via using a planetary mixer (Thinky-ARM 310) for three cycles (30 s per cycle at 2000 rpm). Sudan I dye was added to the nanoparticle suspensions in order to absorb light from the SLA process (see Supporting Information for more details).  $0.08\text{ mg mL}^{-1}$  Sudan I was used for  $\phi_{R202} \geq 0.10$  and  $0.1\text{ mg mL}^{-1}$  for lower concentrations.

**Microscopy:** Transmission electron microscopy (TEM) was performed using an FEI F20 TEM operating at an accelerating voltage of 200 kV. The specimens were prepared by cryo-ultramicrotome (Leica EM UC7/FC7) at  $-70\text{ }^{\circ}\text{C}$  setting the desired thickness to be 100 nm. The slices were then transferred to a copper grid for observation. A Zeiss Gemini 500 scanning electron microscope was used to characterize the surface of printed demos at an accelerating voltage of 1 or 1.5 kV. We employed carbon tape and silver paste to fix the sample and sputtered with carbon to minimize charging.

Laser confocal microscopy (LCM) was performed using a Keyence VK-X260 LCM to characterize the roughness of printed demos. The sample surfaces were scanned under a  $10\times$  objective and the data were processed via MultiFileAnalyzer.

**Photochemistry Measurements:** Using oscillatory photorheology (DHR3, TA instruments; Omnicure Series 1500 light source with a bandpass filter, wavelength,  $400\text{ nm} < \lambda < 500\text{ nm}$ , Lumen Dynamics) at a fixed frequency ( $f = 1\text{ s}^{-1}$ ) and strain ( $\gamma = 0.01$ ), the photocuring behavior of the suspensions was characterized. The gelation point, or transition from liquid resin to solid polymer, was inferred as the photoirradiation dosage where storage modulus ( $G'$ ) climbs above the loss modulus ( $G''$ ).

Additionally, the photochemistry was investigated using a Q1000 modulated photo-differential scanning calorimeter (photo-DSC, TA Instruments, DE, USA), coupled with the same light source used for photorheology. In these tests, identical fiber optic cables guided a  $10\text{ mW cm}^{-2}$  light beam to a pan containing a known mass of resin and an empty reference pan. The difference in heat flow was due to the exothermic thiol-ene photocrosslinking.

**Rheology Measurements:** To characterize the viscoelasticity of the liquid silicone resins, shear viscosity measurements (shear rate,  $0.01 \leq \dot{\gamma} \leq 1000\text{ s}^{-1}$ ) were carried out using a cone-plate (50 mm diameter) geometry of the MCR 702 (Anton Paar, Graz, Austria) rheometer. The yield stress of different resins was further assessed by performing a strain sweep from  $10^{-4} < \gamma < 1$  at  $f = 0.1\text{ s}^{-1}$  with a concentric cylinder geometry on the DHR3 rheometer. To characterize frequency response of different resins and calculate  $Pe$ , a frequency sweep was conducted at  $\gamma = 0.01$  on the MCR 702 rheometer from  $0.1 < \omega < 500\text{ rad s}^{-1}$  and the high frequency viscosity,  $\mu_{\infty}$ , was deduced. The temperature-dependent viscosity of the suspensions at  $\gamma = 0.01$  and  $f = 1\text{ s}^{-1}$  was measured, from  $30 < T < 100\text{ }^{\circ}\text{C}$ , at a ramp rate of  $1\text{ }^{\circ}\text{C min}^{-1}$ .

**Mechanical Tests:** To test the mechanical properties of the cured elastomers, the suspensions were poured into dog-bone shaped molds (width = 6.4 mm, depth = 3.0 mm, gage length = 40 mm) and they were photocured using an Omnicure 1500 UV light source (Lumen dynamics). Uniaxial tensile tests were performed with a Zwick & Roell Z1010 testing machine (Ulm, Germany) using a strain rate of  $1.0\text{ min}^{-1}$  until failure. Cyclic tests of the neat 5% VS6000 and silica (R202) filled composite-silicones were performed, using the same Zwick & Roell tester, to measure the viscoelasticity and material fatigue. In the cyclic tests, these dog-bone shaped samples were stretched to  $\approx 0.6$  of their previously measured  $\gamma_{ult}$  ( $\gamma$  from  $\approx 0.4$  to  $\approx 0.9$  for the neat and silica filled silicones, respectively) and relaxed to the preload force at a controlled strain rate of  $\dot{\gamma} \approx 1.0\text{ min}^{-1}$ . Each sample was loaded cyclically for more than ten times. In addition, for selecting the ideal nanofiller, the silicone composites were cured with different silica nanofillers to round disks ( $\approx 10\text{ mm}$  diameter) with the Omnicure 1500 UV lamp, and oscillatory strain amplitude sweeps were performed from  $10^{-3} < \gamma < 5$  under fixed  $f = 1\text{ s}^{-1}$ , using a DHR3 rheometer (TA Instruments, New Castle, DE, USA).

**UV-Vis Spectroscopy:** To assess the absorption spectra of the silica-silicone suspensions, a UV-vis plate reader (Molecular Devices, San Jose, CA) scanning from 300 to 750 nm was used. In addition, the emission spectra were collected from 350 to 750 nm after excitation at 410 nm (a similar spectrum to the light source within the SLA printer).

**DLS of Tough Silicone:** The materials were 3D-printed using a modified desktop printer (Autodesk Ember; San Rafael, CA, USA) based on a blue LED projector ( $\lambda = 405\text{ nm}$  and  $E = 22.5\text{ mW cm}^{-2}$ ) similar to the previously reported work.<sup>[17]</sup> In the modified printer, a transparent polymethylpentene (PMP) window was used, which allowed

for low adhesion forces and restricted build-head movement only in the  $z$  direction, to reduce overall print time and potential printing resolution errors from fluid momentum. Briefly, the printing file was first imported, which was obtained for free from the web and modified using Solidworks, into the Ember printer. The printing parameters were set up using Print Studio software. After loading the vat with newly prepared resin ( $\approx 50$  mL), printing was done with layer thickness of 30 or 50  $\mu\text{m}$ . Instead of applying vat rotation for layer delamination, the ongoing print was allowed to directly pull up from the PMP window for layer separation. Also, the optical dosage for resins were tuned with different  $\phi_{R202}$  based on their curing rate, for consistent printing resolution. After printing, the parts were rinsed with isopropanol for a few times to remove any residual resin.

**Heating-Assisted DLS:** For heating-assisted DLS, Ni-Cr wire (resistance,  $R = 2.5 \Omega$ ; McMaster-Carr, Elmhurst, IL, USA) was cut and it was coiled manually as the heating module. When heating the resin, the voltage of a DC power supply (1745 A, B&K Precision Co., Yorba Linda, CA, USA) was set as 8 V, so the total heating power was about 25 W. Before each printing, the resin was equilibrated for 10 min so that its temperature around the window area was a uniform  $T \approx 60^\circ\text{C}$ , measured by an infrared camera (E5, FLIR Systems, Wilsonville, OR, USA).

## Supporting Information

Supporting Information is available from the Wiley Online Library or from the author.

## Acknowledgements

K.W. and W.P. contributed equally to this work. This work made use of the Cornell Center for Materials Research Shared Facilities which are supported through the NSF MRSEC program (DMR-1719875). The authors thank Philip Carubia for assistance on rheology tests. The 3D printers received from Autodesk are also greatly appreciated

## Conflict of Interest

The authors declare no conflict of interest.

## Keywords

3D printing, nanocomposites, rheology, stereolithography, suspensions

Received: March 8, 2020

Revised: April 23, 2020

Published online:

- 
- [1] C. Majidi, *Soft Rob.* **2014**, *1*, 5.  
 [2] F. Ilievski, A. D. Mazzeo, R. F. Shepherd, X. Chen, G. M. Whitesides, *Angew. Chem., Int. Ed.* **2011**, *50*, 1890.  
 [3] R. T. Shafraneck, S. C. Millik, P. T. Smith, C.-U. Lee, A. J. Boydston, A. Nelson, *Prog. Polym. Sci.* **2019**, *93*, 36.  
 [4] D. Rus, M. T. Tolley, *Nature* **2015**, *521*, 467.  
 [5] M. T. Tolley, R. F. Shepherd, B. Mosadegh, K. C. Galloway, M. Wehner, M. Karpelson, R. J. Wood, G. M. Whitesides, *Soft Rob.* **2014**, *1*, 213.  
 [6] K. E. Polmanteer, *Rubber Chem. Technol.* **1988**, *61*, 470.  
 [7] K. J. Quinn, J. M. Courtney, *Br. Polym. J.* **1988**, *20*, 25.  
 [8] J. C. McDonald, G. M. Whitesides, *Acc. Chem. Res.* **2002**, *35*, 491.

- [9] D. Trivedi, C. D. Rahn, W. M. Kier, I. D. Walker, *Appl. Bionics Biomech.* **2008**, *5*, 99.  
 [10] K. Tian, J. Bae, S. E. Bakarich, C. Yang, R. D. Gately, G. M. Spinks, M. In Het Panhuis, Z. Suo, J. J. Vlassak, *Adv. Mater.* **2017**, *29*, 1604827.  
 [11] C. Hamilton, K. Tian, J. Bae, C. Yang, G. Alici, G. M. Spinks, Z. Suo, J. J. Vlassak, M. In Het Panhuis, *MRS Adv.* **2018**, *3*, 1597.  
 [12] M. Li, K. G. Neoh, L. Q. Xu, R. Wang, E.-T. Kang, T. Lau, D. P. Olszyna, E. Chiong, *Langmuir* **2012**, *28*, 16408.  
 [13] J. Zhou, A. V. Ellis, N. H. Voelcker, *Electrophoresis* **2010**, *31*, 2.  
 [14] D. Qin, Y. Xia, G. M. Whitesides, *Nat. Protoc.* **2010**, *5*, 491.  
 [15] T. Fujii, *Microelectron. Eng.* **2002**, *61-62*, 907.  
 [16] B. N. Peele, T. J. Wallin, H. Zhao, R. F. Shepherd, *Bioinspiration Biomimetics* **2015**, *10*, 055003.  
 [17] T. J. Wallin, J. H. Pikul, S. Bodkhe, B. N. Peele, B. C. Mac Murray, D. Therriault, B. W. McEnerney, R. P. Dillon, E. P. Giannelis, R. F. Shepherd, *J. Mater. Chem. B* **2017**, *5*, 6249.  
 [18] J. M. Serrine, V. Meenakshisundaram, N. G. Moon, P. J. Scott, R. J. Mondschein, T. F. Weiseman, C. B. Williams, T. E. Long, *Polymer* **2018**, *152*, 25.  
 [19] C. J. Thrasher, J. J. Schwartz, A. J. Boydston, *ACS Appl. Mater. Interfaces* **2017**, *9*, 39708.  
 [20] Smooth-On, Ecoflex Series, [https://www.smooth-on.com/tb/files/ECOFLEX\\_SERIES\\_TB.pdf](https://www.smooth-on.com/tb/files/ECOFLEX_SERIES_TB.pdf), accessed: 12, **2019**.  
 [21] J. Koo, *Fundamentals, Properties, and Applications of Polymer Nanocomposites*, Cambridge University Press, Cambridge, UK **2015**.  
 [22] D. E. Hanson, M. Hawley, R. Houlton, K. Chitanvis, P. Rae, E. B. Orler, D. A. Wroblewski, *Polymer* **2005**, *46*, 10989.  
 [23] H. Li, L. Yang, G. Weng, W. Xing, J. Wu, G. Huang, *J. Mater. Chem. A* **2015**, *3*, 22385.  
 [24] H. Alamri, I. M. Low, *Mater. Des.* **2012**, *42*, 214.  
 [25] L. Bokobza, *J. Appl. Polym. Sci.* **2004**, *93*, 2095.  
 [26] M. J. Wang, M. D. Morris, Y. Kutsovsky, *KGK, Kautsch. Gummi Kunstst.* **2008**, *61*, 107.  
 [27] E. Delebecq, N. Hermeline, A. Flers, F. Ganachaud, *ACS Appl. Mater. Interfaces* **2012**, *4*, 3353.  
 [28] V. M. Kopylov, E. I. Kostyleva, I. M. Kostylev, A. V. Koviadin, *Int. Polym. Sci. Technol.* **2011**, *38*, 35.  
 [29] I. M. Krieger, T. J. Dougherty, *Trans. Soc. Rheol.* **1959**, *3*, 137.  
 [30] C. Hinczewski, S. Corbel, T. Chartier, *Rapid Prototyping J.* **1998**, *4*, 104.  
 [31] T. J. Wallin, J. Pikul, R. F. Shepherd, *Nat. Rev. Mater.* **2018**, *3*, 84.  
 [32] Z. C. Eckel, C. Zhou, J. H. Martin, A. J. Jacobsen, W. B. Carter, T. A. Schaedler, *Science* **2016**, *351*, 58.  
 [33] B. Zhang, W. Zhang, Z. Zhang, Y.-F. Zhang, H. Hingorani, Z. Liu, J. Liu, Q. Ge, *ACS Appl. Mater. Interfaces* **2019**, *11*, 10328.  
 [34] S. C. Ligon, R. Liska, J. Stampfl, M. Gurr, R. Mülhaupt, *Chem. Rev.* **2017**, *117*, 10212.  
 [35] T. Chartier, A. Badev, Y. Abouliatim, P. Lebaudy, L. Lecamp, *J. Eur. Ceram. Soc.* **2012**, *32*, 1625.  
 [36] D. T. Pham, C. Ji, *Proc. Inst. Mech. Eng., Part C* **2003**, *217*, 105.  
 [37] J. R. Tumbleston, D. Shirvanyants, N. Ermoshkin, R. Januszewicz, A. R. Johnson, D. Kelly, K. Chen, R. Pinschmidt, J. P. Rolland, A. Ermoshkin, E. T. Samulski, J. M. DeSimone, *Science* **2015**, *347*, 1349.  
 [38] D. A. Walker, J. L. Hedrick, C. A. Mirkin, *Science* **2019**, *366*, 360.  
 [39] T. Zhao, R. Yu, S. Li, X. Li, Y. Zhang, X. Yang, X. Zhao, C. Wang, Z. Liu, R. Dou, W. Huang, *ACS Appl. Mater. Interfaces* **2019**, *11*, 14391.  
 [40] A. K. Gaharwar, C. P. Rivera, C. J. Wu, G. Schmidt, *Acta Biomater.* **2011**, *7*, 4139.  
 [41] Evonik Industries AG, AEROSIL – Fumed Silica Technical Overview, <https://www.aerosil.com/sites/lists/RE/DocumentsSI/Technical-Overview-AEROSIL-Fumed-Silica-EN.pdf>, accessed: 01, **2020**.  
 [42] D. R. Paul, J. E. Mark, *Prog. Polym. Sci.* **2010**, *35*, 893.

- [43] J. Jordan, K. I. Jacob, R. Tannenbaum, M. A. Sharaf, I. Jasiuk, *Mater. Sci. Eng., A* **2005**, 393, 1.
- [44] L. Xia, Z. Xu, L. Sun, P. M. Caveney, M. Zhang, *J. Nanopart. Res.* **2013**, 15, 1570.
- [45] L. Yan, D. A. Dillard, R. L. West, L. D. Lower, G. V. Gordon, *J. Polym. Sci., Part B: Polym. Phys.* **2010**, 48, 2207.
- [46] J. E. Smay, G. M. Gratson, R. F. Shepherd, J. Cesarano, J. A. Lewis, *Adv. Mater.* **2002**, 14, 1279.
- [47] M. T. Roberts, A. Mohraz, K. T. Christensen, J. A. Lewis, *Langmuir* **2007**, 23, 8726.
- [48] W. J. Tseng, K.-C. Lin, *Mater. Sci. Eng., A* **2003**, 355, 186.
- [49] A. R. Studart, E. Amstad, L. J. Gauckler, *Soft Matter* **2011**, 7, 6408.
- [50] T. Shikata, D. S. Pearson, *J. Rheol.* **1994**, 38, 601.
- [51] Q. Huang, N. J. Alvarez, A. Shabbir, O. Hassager, *Phys. Rev. Lett.* **2016**, 087801, 1.
- [52] H. Tabuteau, S. Mora, G. Porte, M. Abkarian, C. Ligoure, *Phys. Rev. Lett.* **2009**, 155501, 1.
- [53] Q. Huang, O. Hassager, *Soft Matter* **2017**, 13, 3470.
- [54] L. Elomaa, S. Teixeira, R. Hakala, H. Korhonen, D. W. Grijpma, J. V. Seppälä, *Acta Biomater.* **2011**, 7, 3850.
- [55] M. L. Williams, R. F. Landel, J. D. Ferry, *J. Am. Chem. Soc.* **1955**, 77, 3701.
- [56] N. Domun, H. Hadavinia, T. Zhang, T. Sainsbury, G. H. Liaghat, S. Vahid, *Nanoscale* **2015**, 7, 10294.